

Nanocrystalline Nd–Fe–B Anisotropic Magnets by Flash Spark Plasma Sintering

Fernando Maccari,* Tarini Prasad Mishra, Monica Keszler, Tobias Braun, Esmaeil Adabifiroozjaei, Iliya Radulov, Tianshu Jiang, Enrico Bruder, Olivier Guillon, Leopoldo Molina-Luna, Martin Bram,* and Oliver Gutfleisch


Flash spark plasma sintering (flash SPS) is an attractive method to obtain Nd–Fe–B magnets with anisotropic magnetic properties when starting from melt-spun powders. Compared to the benchmark processing route via hot pressing with subsequent die upsetting, flash SPS promises electroplasticity as an additional deformation mechanism and reduced tool wear, while maximizing magnetic properties by tailoring the microstructure—fully dense and high texture. A detailed parameter study is conducted to understand the influence of Flash SPS parameters on the densification and magnetic properties of commercial MQU-F powder. It is revealed that the presintering conditions and preheating temperature before applying the power pulse play a major role for tailoring grain size and texture in the case of hot deformation via Flash SPS. Detailed microstructure and magnetic domain evaluation disclose the texture enhancement with increasing flash SPS temperature at the expense of coercivity. The best compromise between remanence and coercivity (1.37 T and 1195 kA m⁻¹, respectively) is achieved through a combination of presintering at 500 °C for 120 s and preheating temperature of 600 °C, resulting in a magnet with energy product (BH)_{max} of 350 kJm⁻³. These findings show the potential of flash SPS to obtain fully dense anisotropic nanocrystalline magnets with high magnetic performance.

1. Introduction

Due to having the highest maximum energy-product (BH)_{max} (theoretical 512 kJm⁻³) of all permanent magnet materials currently available on the market, Nd–Fe–B magnets are indispensable for manifold applications such as wind turbines, electric vehicles, hybrid electric vehicles, e-bikes, consumer electronics, computers, and other green energy technologies.^[1–3] The amount of Nd–Fe–B magnets needed for these applications varies in the range from few grams in consumer electronics to tons for large turbines.^[4] High-performing applications like traction motors require Nd–Fe–B magnets that combine high remanence (B_r), high coercivity (H_{c_j}), and temperature stability. The magnetization of a magnet directly depends on the volume fraction of the hard magnetic phase. Therefore, maximize density and decrease of secondary phase or binder contents are effective measures to maximize this value. In the case of anisotropic magnets, exact

F. Maccari, T. Braun, I. Radulov, O. Gutfleisch
Institute of Materials Science
Functional Materials
Technical University of Darmstadt
64287 Darmstadt, Germany
E-mail: fernando.maccari@tu-darmstadt.de

T. P. Mishra, M. Keszler, O. Guillon, M. Bram
Institute of Energy and Climate Research, Materials Synthesis and
Processing (IEK-1)
Forschungszentrum Jülich GmbH
52425 Jülich, Germany
E-mail: m.bram@fz-juelich.de

 The ORCID identification number(s) for the author(s) of this article can be found under <https://doi.org/10.1002/adem.202300252>.

© 2023 The Authors. Advanced Engineering Materials published by Wiley-VCH GmbH. This is an open access article under the terms of the Creative Commons Attribution-NonCommercial-NoDerivs License, which permits use and distribution in any medium, provided the original work is properly cited, the use is non-commercial and no modifications or adaptations are made.

DOI: 10.1002/adem.202300252

E. Adabifiroozjaei, T. Jiang, L. Molina-Luna
Institute of Materials Science
Advanced Electron Microscopy
Technical University of Darmstadt
64287 Darmstadt, Germany

I. Radulov, O. Gutfleisch
Fraunhofer Research Institution for Materials Recycling and Resource
Strategies IWKS
63457 Hanau, Germany

E. Bruder
Institute of Materials Science, Physical Metallurgy
Technical University of Darmstadt
64287 Darmstadt, Germany

O. Guillon
Jülich Aachen Research Alliance, JARA-Energy
52425 Jülich, 52066 Aachen, Germany

M. Bram
Institut für Werkstoffe
Ruhr-Universität Bochum
44801 Bochum, Germany

alignment along the easy magnetization axis (which, in Nd₂Fe₁₄B, is the *c* crystallographic axis) of each grain to the magnetization direction is another important factor for maximizing the remanence and (BH)_{max}. For maximizing coercivity, the most common technique is the addition of heavy rare-earth elements (HREEs) to increase anisotropy field, such as Dy and Tb, and the use of other elements like Ga, Cu, and Al, which promote magnetic grain isolation by the formation of nonmagnetic phases at grain boundaries.^[5–10] However, HREEs decrease the magnetization, and their use becomes increasingly critical due to price, abundance, and geopolitical reasons.^[11–14] Recently, the grain-boundary diffusion process has been developed to effectively reduce the HREE amount without loss of coercivity.^[15,16] As an alternative, hot-deformed Nd–Fe–B magnets have the potential to avoid HREEs due to their high anisotropic microstructure and grain size in the range of critical single-magnetic domain ($D_c \approx 300$ nm), but exact microstructure control during hot deformation is a challenging task.^[17–22]

There are different processing routes for fabricating Nd–Fe–B magnets optimized with respect to the energy product on industrial scale.^[23] In general, all routes are based on powder metallurgy. The routes can be categorized by whether they result in microcrystalline or nanocrystalline magnets. Microcrystalline Nd–Fe–B magnets are traditional powder metallurgical products.^[4,24] Powder production starts by casting an ingot containing the required alloying elements. The ingot is pulverized with a coarse grind/hydrogen decrepitation and then jet-milled, resulting in a powder with a mean particle size in the range of 1–10 μm. Shaping of the powder can be done by pressing, extrusion, or injection molding. Before or during compaction, the powder particles have to be aligned in a magnetic field of around 10–20 kOe. Consolidation of the parts is done by liquid-phase sintering at temperatures around 1000–1100 °C. Higher amounts of rare-earth elements support formation of liquid phase and suppress α-Fe precipitation. An optional post-thermal treatment at around 600 °C is done to further increase coercivity by improving the wettability of the grain-boundary phase and magnetically decouple the hard magnetic grains. For processing of nanocrystalline magnets, a melt containing the alloying elements is melt-spun resulting in ribbons or flakes with a size of few 100 μm. For better handling of the powders, the size of the ribbons can be diminished by crushing. Due to extremely rapid solidification, the primary grain size of the Nd₂Fe₁₄B phase remains in the nanometer range (primary grain size in the range of 10–30 nm,^[22] while still containing amorphous portions. Alternative ways of producing nanometer-scaled Nd–Fe–B powders include gas atomization,^[25] hydrogenation–disproportionation–desorption–recombination^[26–28] and mechanically alloying.^[29,30] Nanocrystalline Nd–Fe–B powders can be either directly applied in polymer-bonded magnets or be used as starting materials for hot-compaction/deformation processes. The standard hot-deformation route is established in industry and contains the following steps.^[18,20,22,31–33] First, the powder is cold-pressed at room temperature using a uniaxial or cold isostatic press. Then, the pre-compact is hot-pressed to almost fully density at temperatures in the range of 650–900 °C and pressure up to 300 MPa.^[32,33] In the as hot-pressed state, the microstructure consists of randomly aligned, rounded grains with a size in the range of 20–50 nm, resulting in isotropic magnetic

properties. The final and most challenging step is the hot deformation at which a thermomechanical alignment of the primary grains occurs. Depending on the hot-deformation parameters (usually done at temperatures between 650 and 900 °C, pressure up to 100 MPa, height reduction up to 70%,^[22,32,33] grain size, and diameter/height aspect ratio can be tuned, resulting in plate-like grains with widths in the range of 200–500 nm and grain thicknesses in the range of 20–50 nm. Again, addition of alloying elements like Ga, along with hyperstoichiometric RE composition, can be helpful for supporting the hot-deformation step through the formation of a transient liquid phase. To take advantage of liquid-phase-supported sintering/deformation, hot-pressing and hot deformation must be done above the specific transient liquidus temperature of the grain-boundary phase, which is typically above 655 °C.^[34–36] However, temperatures that are too high can cause abnormal grain growth, leading to a decrease of coercivity. Ultimately, the desired microstructure comprises platelike Nd₂Fe₁₄B nano-grains (critical single-domain size) with fiber texture along the *c* axis, which are magnetically isolated by a thin Nd-rich grain-boundary phase. Established methods of hot deformation are either die-upsetting (deformation of the hot-pressed body in a uniaxial press) or hot extrusion.^[37] The latter is applied, for example, for production of ring-shaped magnets. In general, hot deformation requires advanced processing technology and expensive tooling, leading to significantly enhanced processing costs when compared to polymer-bonded or conventionally sintered magnets.^[20,38]

Electric current-assisted sintering (ECAS) is an attractive alternative for the hot deformation of nanocrystalline Nd–Fe–B magnets with pronounced anisotropic magnetic properties. It is expected that direct current flow through a pre-compacted Nd–Fe–B powder compound activates additional deformation and sintering mechanisms not accessible by conventional processing. There are hypotheses that the occurrence of electroplasticity^[39,40] is a key factor in decreasing the deformation load, resulting in reduced tool wear and enhanced deformation degree.^[41] In combination with controlled adjustment of microstructure, reducing the amount of HREEs without loss of magnetic performance therefore becomes a possibility.^[42] Furthermore, recent investigations reveal that hot-pressing of dense Nd–Fe–B compacts is not necessarily required as an intermediate processing step, making ECAS technologies attractive for direct recycling of scrap from hot-deformed magnets.^[43,44] From the ECAS family,^[45] three technologies are most promising for the manufacturing of Nd–Fe–B magnets. Up to now, proof of concept has only been achieved on lab scale in all cases. 1) Electro-discharge sintering is a rapid and economic ECAS process, which enables extremely high heating rates up to 10⁶ Kmin^{−1} by the sudden release of energy stored in a capacitor bank via the powder. For direct Joule heating of the powder, the tool consists of conductive punches made of a copper alloy and a nonconducting die, therefore forcing the current pulse through the powder bed. Almost full densification of Nd–Fe–B powders has been achieved within milliseconds.^[43,46,47] Nevertheless, the resulting microstructure lacks homogeneity, exhibiting fully densified, partly densified, and remelted zones. Due to lack of high deformation of the primary grains and microstructural inhomogeneity, only isotropic magnetic properties were demonstrated so far (remanence B_r of 0.78 T, coercivity H_{ci} of 1565 kAm^{−1}, and

energy product $(BH)_{\max}$ of 102 kJm^{-3} .^[46] 2) Field-assisted sintering technology/spark plasma sintering (FAST/SPS) is a low-voltage, current-activated, and pressure-assisted sintering process characterized by high heating rates and short cycle times.^[40,48] Powders are filled in a conductive tool heated by the Joule effect. Usually, graphite is used as tool material. For conductive materials like Nd–Fe–B, indirect heating by thermal conduction is supported by direct Joule heating of the powder compact. FAST/SPS can be used to replace the hot-pressing step resulting in isotropic Nd–Fe–B magnets as demonstrated, for example, by Wüst et al.^[49] Going a step further, FAST/SPS can be also used for die-upsetting. Wang et al. produced a Nd–Fe–B magnet with a remanence B_r of 1.42 T, a coercivity H_{ci} of 1234 kAm^{-1} , and a maximum energy product of 385.9 kJm^{-3} by FAST/SPS without exactly specifying experimental setup and parameters.^[50] Several other authors report the application of FAST/SPS for the production of anisotropic Nd–Fe–B magnets.^[51–56] 3) Flash spark plasma sintering (Flash SPS) is a specific kind of operation mode possible in conventional FAST/SPS devices.^[57] A high-power-current pulse of defined length (usually only a few seconds) is forced through the sample. Our recent study reveals that preheating of the sample before applying the power pulse further improves the deformation.^[44] For conducting Flash SPS cycles, the sample is placed between the punches of the FAST/SPS device enabling to apply a defined load during the current pulse. As such, Flash SPS is characterized by a simultaneous densification and hot deformation of the sample with large height reduction in very short time, enabling pronounced crystallographic texture while keeping the grain size on nanometer scale. Castle et al. demonstrated the potential of Flash SPS by producing an anisotropic Nd–Fe–B magnet starting from a Dy-free melt-spun Nd–Fe–B powder (Magnequench MQU-F).^[42,58] With optimized parameters, a remanence B_r of 1.16 T, a coercivity H_{ci} of 1438 kAm^{-1} and energy product $(BH)_{\max}$ of 230 kJm^{-3} was achieved.

In our recent work, FAST/SPS and Flash SPS were evaluated and benchmarked regarding the production of dense isotropic and anisotropic Nd–Fe–B magnets.^[44] Commercial Nd–Fe–B powder (Magnequench MQU-F) was used as starting material. As expected, conventional FAST/SPS is preferentially suitable for the production of isotropic magnets. Application of optimized parameters (heating rate 100 K min^{-1} , temperature $700 \text{ }^\circ\text{C}$, dwell time 30 s, and pressure 50 MPa) resulted in a remanence B_r of 0.84 T, a coercivity H_{ci} of 1683 kAm^{-1} , and energy product $(BH)_{\max}$ of 123 kJm^{-3} . For conducting Flash SPS cycles, samples had to be pre-sintered to withstand the minimum load of 10 kN (=32 MPa for \varnothing 20 mm samples) required for operation of the Flash SPS equipment used in this study. Pre-sintering was done by FAST/SPS (heating rate 100 K min^{-1} , temperature $500 \text{ }^\circ\text{C}$, dwell time 30 s, and pressure 50 MPa) resulting in a density of around 70%. Flash SPS parameter optimization focused on the hot-deformation step while the preheating parameters of the samples were kept constant ($300 \text{ }^\circ\text{C}$, 120 s, 32 MPa). The best magnetic properties (remanence B_r 1.18 T, coercivity H_{ci} 1483 kAm^{-1} , energy product $(BH)_{\max}$ 264 kJm^{-3}) were achieved by applying a defined power pulse of 35 kW for 30 s while keeping the minimum possible pressure of 32 MPa. A remarkable output of this study was the successful densification of magnet

scrap from commercial hot-deformed magnets, which is not possible with the established processing routes.

In the present work, the influence of two processing parameters on microstructure evolution and magnetic properties of Flash SPS samples was studied in detail. For comparability, all experiments were done with the same type of powder as in the former study (Magnequench MQU-F).^[44] On the one hand, pre-sintering of the powder compacts were done via FAST/SPS at $500 \text{ }^\circ\text{C}$ varying the dwell time to 30 and 120 s. In addition to enhance the stability of the powder compacts, our hypothesis is that pre-sintering with longer dwell time leads to the formation of more pronounced sintering necks between the primary particles retarding the grain growth at a later stage of the Flash SPS cycle. On the other hand, preheating temperature systematically varied between $251 \text{ }^\circ\text{C}$ (minimum pyrometer reading) and $600 \text{ }^\circ\text{C}$ while keeping the load (32 MPa) and dwell time constant (120 s). Afterward, the final Flash SPS step was done using the same parameter set for all samples (32 MPa, 35 kW, and 30 s). Flash SPS cycles were still done without an outer die leading to a frayed sample edge with some cracks. The difference of magnetic properties between the center and the edge of the sample is discussed. The study helped to gain a better understanding of the relationship between Flash SPS parameters, resulting in microstructure and magnetic properties. Compared to our former study,^[44] magnetic properties could be significantly improved (Remanence B_r 1.37 T, coercivity H_{ci} 1195 kAm^{-1} , energy product $(BH)_{\max}$ 350 kJm^{-3}). In sum, the study enabled us to gain a better understanding how Flash SPS parameters influence final microstructure and magnetic properties.

2. Experimental Section

2.1. Starting Powders

Commercial melt-spun Nd–Fe–B powder (MQU-F, Lot. B33077) from Magnequench was used as the starting material. The ribbons had a size of up to $400 \text{ }\mu\text{m}$ and contained primary nanocrystalline grains with a size about 50 nm. Figure S1, Supporting Information, shows the flake-like morphology resulting from the melt spinning and grinding processes. Figure S2, Supporting Information, shows the particle-size distribution of the melt-spun flakes. The tap density of the flakes was 46% aggravating the homogeneous filling of the FAST/SPS tool for pre-sintering. The nominal composition of the powder was 30.0% Nd, 5.88% Co, 0.60% Ga, 0.92% B (all values in wt%), and Fe as balance. In the alloy, Co replaces Fe in the hard-magnetic-phase order to increase the Curie temperature without significantly changing remanence and coercivity, while improving the corrosion resistance of the grain-boundary phase.^[59] Alloying with Ga is effective in the grain-boundary phase and improves the workability during hot deformation and contributes to magnetic isolate the hard magnetic grains. Furthermore, the alloy is almost free of the critical HREE, Dy.

2.2. Pre-Sintering of Nd–Fe–B Powder by FAST/SPS

All samples in the present study were pre-sintered by FAST/SPS. FAST/SPS cycles were performed in an HP D5 device (FCT

Systeme, Rauenstein, Germany) in vacuum. The Nd–Fe–B flakes/powder of 15 g, in the as-received state, were poured into a graphite die (SGL Carbon, SIGRAFINE R7710) with an inner diameter of 20 mm. A graphite foil (SGL Carbon, SIGRAFEX) with a thickness of 0.35 mm was inserted for improving the contact between tool and sample. The FAST/SPS parameters were kept constant (heating rate 100 K min^{-1} , maximum temperature $500 \text{ }^\circ\text{C}$, pressure 50 MPa) with exception of the holding time at maximum temperature, which was 30 s for series A and 120 s for series B. The pre-sintering conditions were chosen to safely avoid the formation of any melting phase at this stage and therefore to suppress grain growth already during pre-sintering. Figure S3, Supporting Information, shows the DSC curve of the starting powder confirming that there is no melting phase formation at $500 \text{ }^\circ\text{C}$. The load-temperature-displacement curves of samples pre-sintered at $500 \text{ }^\circ\text{C}$ for 30 and 120 s is given in Figure S4, Supporting Information. The goal of varying the dwell time was to achieve a more pronounced formation of sintering necks between the primary particles for the longer dwell time, which is expected to retard abnormal grain growth during Flash SPS. The relative density of the pre-sintered samples was calculated by geometrical means, showing a variation between 70% and 77%. However, the samples with longer pre-sintering time showed higher mechanical integrity, while the samples from the series A were fragmented in small pieces during cutting for further characterization. The pre-sintering step was beneficial for stabilizing the samples from both series when mounting them in the Flash SPS setup.

2.3. Flash SPS of Pre-Sintered Nd–Fe–B Pellets

All Flash SPS cycles were conducted in a hybrid FAST/SPS device (H-HP-D 25 SD/FL/MoSi from FCT Systeme GmbH, Rauenstein, Deutschland). For conducting Flash SPS, pre-sintered pellets were placed between two graphite punches (diameter 60 mm) with plane-parallel surfaces. The samples had a direct contact to the face of the punches and all experiments were done without an outer die. Therefore, the sample

edge was frayed after Flash SPS (Figure S5, Supporting Information). The minimum load of 10 kN ($=32 \text{ MPa}$ for $\varnothing 20 \text{ mm}$ samples) was required for enabling the operation of the abovementioned FAST/SPS device. Amongst others, the pre-load improved the electrical contact. For more information on the experimental setup, we refer to our recent work.^[44] Before applying the Flash SPS pulse, samples were preheated via direct Joule heating. In the present study, the preheating temperature was varied to 251, 300, 400, 500, and $600 \text{ }^\circ\text{C}$. Figure S6, Supporting Information, shows the related temperature–power–displacement curves of all samples. The preheating temperature was controlled by pyrometer, which measured the temperature at the bottom of a hole drilled in the upper punch. The distance between the bottom of the hole and the sample surface was approximately 4.5 mm. Temperatures below $251 \text{ }^\circ\text{C}$ were omitted since this temperature is the lower temperature bound of the pyrometer used in our device. The power required for preheating increased with increasing preheating temperature. The maximum power for preheating was set to 12 kW, accordingly. The limitation on the maximum heating power during preheating ensured a gradual increment of the sample temperature from room temperature to the respective preheating temperature. After achieving the respective preheating temperature, this temperature was held for 120 s for all samples. When looking at the temperature–power–displacement curves, it becomes obvious that sample displacement already started during preheating if temperature exceeded $300 \text{ }^\circ\text{C}$. At the end of the dwell time, the samples were subjected to a pulse of continuous direct current. For all 10 samples, the maximum heating power and discharge duration of this Flash SPS pulse were fixed to 35 kW and 30 s. All Flash SPS cycles were done with the minimum accessible load of 10 kN (32 MPa). Table 1 summarizes the parameter sets of series A and series B samples.

2.4. Characterization

Particle-size distribution of the powder flakes was measured by sieve analysis and is given as Supporting Information (Figure S1,

Table 1. Overview of all samples investigated in this study. All FAST/SPS cycles were conducted with a heating rate of 100 K min^{-1} and a pressure of 50 MPa. Preheating was done setting the maximum heating power to 12 kW. After achieving the specific temperature, it was held for 120 s before applying the Flash SPS power pulse. During preheating and during applying of the power pulse, all samples were loaded with 10 kN ($=32 \text{ MPa}$ at the begin of displacement). The density is relative to a fully dense material, that is, 7.55 g cm^{-3} .

Sample code	FAST/SPS pre-sintering parameters	Relative density [%]	Flash SPS preheating temperature [$^\circ\text{C}$]	Flash SPS power pulse	Relative density [%]
A-30_251	$500 \text{ }^\circ\text{C}$, 30 s	72.4	251	35 kW, 30 s	96.4
A-30_300	$500 \text{ }^\circ\text{C}$, 30 s	71.0	300	35 kW, 30 s	96.8
A-30_400	$500 \text{ }^\circ\text{C}$, 30 s	70.7	400	35 kW, 30 s	98.0
A-30_500	$500 \text{ }^\circ\text{C}$, 30 s	73.9	500	35 kW, 30 s	97.1
A-30_600	$500 \text{ }^\circ\text{C}$, 30 s	70.1	600	35 kW, 30 s	97.9
B-120_251	$500 \text{ }^\circ\text{C}$, 120 s	76.8	251	35 kW, 30 s	96.8
B-120_300	$500 \text{ }^\circ\text{C}$, 120 s	72.7	300	35 kW, 30 s	96.1
B-120_400	$500 \text{ }^\circ\text{C}$, 120 s	73.9	400	35 kW, 30 s	96.5
B-120_500	$500 \text{ }^\circ\text{C}$, 120 s	71.5	500	35 kW, 30 s	95.0
B-120_600	$500 \text{ }^\circ\text{C}$, 120 s	74.8	600	35 kW, 30 s	98.0

Supporting Information). The microstructure of the Flash SPS processed samples was investigated by scanning electron microscopy (SEM) using an field emission gun (FEG)–SEM JEOL JSM-7600 device (JEOL, Japan) operated in secondary electron and backscattered electron modes. Before microstructure characterization, samples were broken into two halves, one was used to investigate the fractured surface. The other half a cross section by grinding with silicon carbide paper and subsequent polishing with water-free, 3 μm , 1 μm , and 0.25 μm diamond suspensions.

For further structural and chemical investigations, thin lamellae were prepared using precision-ion polishing system (Gatan Dual Ion Mill Model 600) and focused-ion beam (JEOL JIB-4600 F) milling, and the lamellae were studied using transmission electron microscope (TEM: JEM-2100, JEOL) in both transmission and scanning transmission modes. The machine was equipped to Oxford X-Max80 EDX detector, thus chemical analysis was also done in scanning transmission mode.

The density of the specimens after Flash SPS was measured by the Archimedes principle. For density calculation, a theoretical density of 7.55 gcm^{-3} was used.

For investigating the formation of a partial melting phase during preheating of the compacts before Flash SPS, a differential scanning calorimetry (DSC) measurement was done in the temperature range from room temperature to 800 $^{\circ}\text{C}$. The measurement was done in a mixture of Ar/He gas flow atmosphere. DSC was done with a Netzsch 404 F1 Pegasus device.

For characterization of the magnetic properties, the samples were cut as shown in **Figure 1** with the aim of evaluating the properties at the center and at the edge. Cuboid samples, with dimensions $1.30 \times 1.30 \times 3.30 \pm 0.1$ mm (larger dimension parallel to the pressing direction), were used for the measurements and for further correction regarding the demagnetization factor. The hysteresis loops were measured using a vibrating sample magnetometer module in a magnetic property measurement system (VSM-MPMS3, Quantum Design, USA) in three different directions for each sample. Measurements were done: 1) parallel to the applied pressure; 2) perpendicular to the applied pressure and radial related to the outer edge; and 3) perpendicular to the applied pressure and tangent to the outer edge, as shown in the schematics in **Figure 1**. All isothermal magnetization

measurements presented in this work are corrected taking the demagnetization factor into consideration.

On selected samples, the domain structure was investigated using Kerr microscopy (Zeiss Axio Imager.D2m, evico magnetics GmbH, Germany) and magnetic force microscopy (MFM Dimension Icon, Bruker, USA). In the latter, a high coercivity cantilever was used (ASYMFMHC-R2, Asylum Research, USA) and a distance between tip and sample surface of 50 nm. The magnetic domain observation plane was parallel to the pressing direction, that is, along the easy magnetization direction.

3. Results and Discussion

3.1. Sample Characterization before Hot Deformation via Flash SPS

All samples were pre-sintered via FAST/SPS at 500 $^{\circ}\text{C}$ and 50 MPa to enhance the mechanical stability for withstanding the preload of 10 kN (32 MPa for a \varnothing 20 mm sample) required for operation of the FAST/SPS device. This preload is specific for the device used in this study (H-HP-D 25 SD/FL/MoSi from FCT Systeme GmbH) and might be optionally omitted in future by adapting the operation conditions of the device accordingly. Nevertheless, low mechanical stability of samples pre-sintered for only 30 s reveal the need of this pre-sintering step for safe handling and mounting the powder compacts in the Flash SPS setup. At the given pre-sintering conditions, a residual porosity in the range of 23–30% remained, and the flakes of the starting powder are still clearly visible in the microstructure (**Figure 2**). The large scattering of porosity of the pre-sintered samples might be caused by the irregular powder shape and the tilt of the particles originating from filling the particles with unfavorable aspect ratio in the die (**Figure S7**, Supporting Information). Nevertheless, there is no clear relation to the densities achieved after the Flash SPS cycle (see **Table 1**).

In the pre-sintered state, formation of sintered bridges between the coarse powder flakes was found (marked by circles in **Figure 2a**, also shown in **Figure S1**, Supporting Information). These bridges are assumed to be the main reason for mechanical stability of the samples after pre-sintering. Furthermore, extended cracking of the powder flakes was observed indicating their brittle nature. As mentioned before, pre-sintering was done with a second intention. By varying the dwell time at 500 $^{\circ}\text{C}$ from 30 s (Series A) to 120 s (Series B), it was aspired to form sintering necks also between the primary particles and to increase the neck size between these primary particles by increase of dwell time from 30 to 120 s. The formation was sintering necks was observed at the samples with longer pre-sintering (120 s), as shown in the bright-field TEM image in **Figure 2b**.

3.2. Comparison of the Magnetic Properties of Flash SPS Samples at the Center and at the Edge

Up to now, all Flash SPS experiments were done without an outer die. Therefore, the diameter of the samples after Flash SPS was not controlled, leading to a frayed outer rim of the samples accompanied by crack formation at the edge.^[44] As expected,

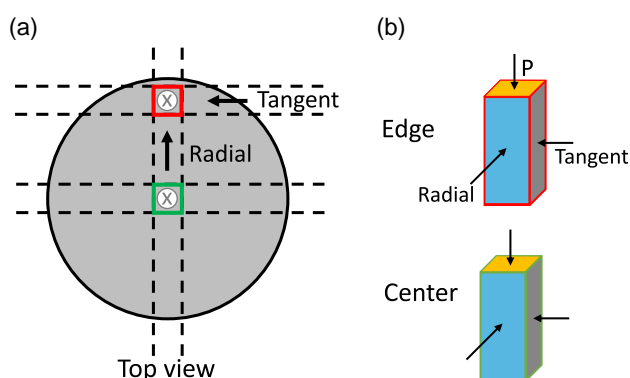


Figure 1. Sample preparation for comparing magnetic properties of the center and the edge. a) Top view and b) definition of directions of magnetic measurements.

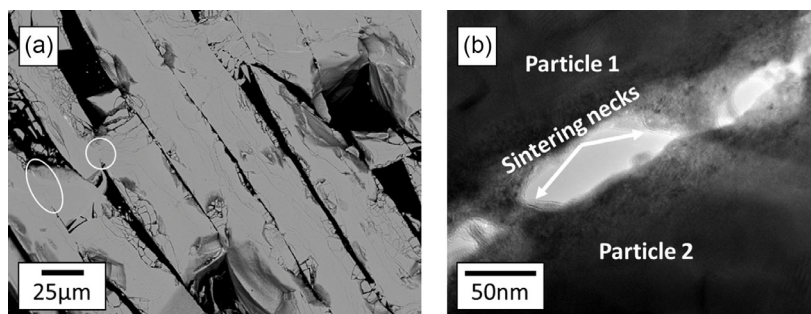


Figure 2. a) Scanning electron microscope (SEM) microstructure of Nd–Fe–B samples after pre-sintering at 500 °C with a dwell time of 120 s. Circles mark the formation of sintered bridges between the coarse melt-spun flakes. Extensive cracking of the flakes hint on their brittle nature. b) Bright-field transmission electron microscope (TEM) image shows the formation of sintering necks between two distinct particles (the difference of magnification of both images is pointed out).

this inhomogeneous macroscopic appearance (Figure S5, Supporting Information) is also reflected on the microscopic level. While in the center of the sample, the former flake-like particles are well aligned and deformed in compaction direction (Figure 3a). At the edge of the sample, the flakes were densified but their alignment and deformation are less pronounced (Figure 3b). Furthermore, an increased amount of residual pores appeared in these areas.

As already known from Nd–Fe–B magnets produced by conventional hot deformation, the interface between former flakes is decorated by a Nd-rich phase, which appears bright in the SEM images.^[18,19,21,60,61] Furthermore, these interfaces are accompanied by a seam of large Nd–Fe–B grains, which are not aligned perpendicular to the pressing direction. Sawatzki et al. explains this specific microstructural detail of hot-deformed magnets as a residual from the melt-spun flakes. During melt spinning, the cooling rate of the melt differs between the face in contact with the water cooled copper wheel and the face in the opposite direction, which is in contact with the surrounding atmosphere.^[62] At areas with lower a cooling rate, a band with significant grain growth of the Nd–Fe–B phase, accompanied by Nd segregation, appears, which remains even after hot deformation—in our case by Flash SPS—and can be clearly seen in Figure 3b. Phase identification was also performed using high-resolution TEM, in which Nd-rich phases (Nd-double hexagonal close-packed (dhcp) and Nd₂O₃) were identified, as shown in Figure S8, Supporting Information. In Figure 4, the interface between two flakes is

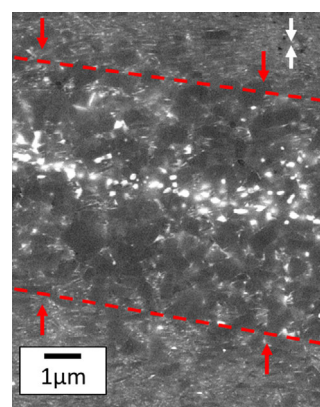


Figure 4. Nd-rich phase concentrated between flakes and grain growth at the interface between former Nd–Fe–B flakes. The pressure direction is given by the white arrows. The red arrows and dashed lines show region with abnormal grain growth.

shown in higher magnification. Here, the slower cooled areas of two flakes are in directed contact. Since the large grains are usually not aligned to the compaction direction, they do not contribute to the aspired anisotropic magnetic behavior.^[62]

Figure 5 exemplarily shows the influence of position and orientation on the magnetic properties. As already demonstrated before,^[42,44] hot deformation via Flash SPS enables the

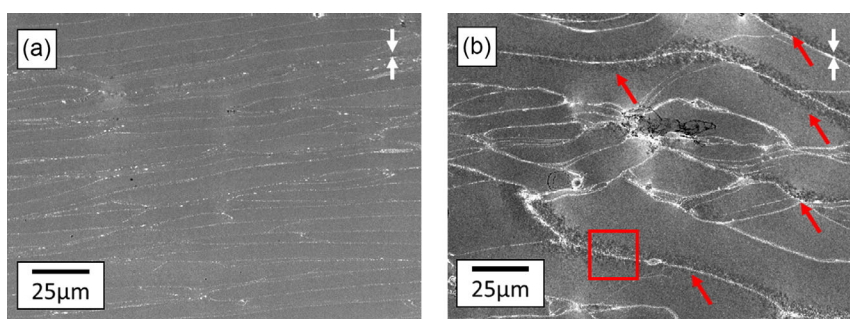


Figure 3. Microstructure of Nd–Fe–B sample B-120_500: a) center and b) edge—red marked area is shown in higher magnification in Figure 4. The pressure direction is given by the white arrows. The red arrow shows regions with abnormal grain growth.

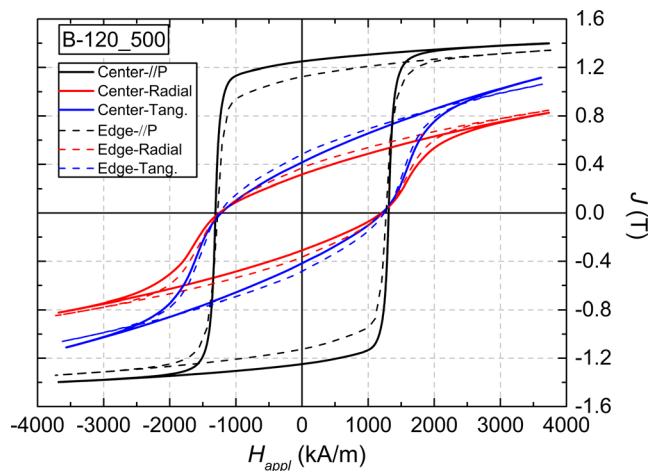


Figure 5. Difference of magnetic properties, measured along different directions, between center and edge on the example of the sample B-120_500.

production of Nd–Fe–B magnets with well-pronounced magnetic anisotropy. Up to now, there was no detailed information regarding how the magnetic properties vary when comparing the center and the edge of the samples. As shown in Figure 3, the deformation and alignment of the former powder flakes in the deformation direction is less pronounced at the edge, as shown by the difference between the parallel direction and both perpendicular directions (Tangent and Radial). An explanation of the reduced remanence is that the zone with coarse Nd–Fe–B grains, which are not aligned to the compaction direction, seems to become enlarged at the edge. A reason for this behavior could be a lower cooling rate at the edge due to a combination of conducting the Flash SPS cycle without an outer die in the present work in and the possibility of inhomogeneous deformation throughout the sample.^[22] However, there is an almost constant coercivity in all directions at the center and edge. This behavior hints to be a trade-off between the influence of grain size—larger grain size leads to lower coercivity—and the angular dependence on the coercivity values. It is explained in the literature that randomly oriented grains show higher coercivity.^[22,63] Moreover, the small difference observed in the shape and in the remanence between radial and tangent directions indicates that there is a deviation from the ideal fiber texture, leading to a misorientation variation within both perpendicular directions.

From the results, it becomes obvious that further improvement of the Flash SPS process—among others, by conducting the Flash SPS cycles with an outer die to better control the cooling and the outer shape of the magnet—is mandatory to manufacture magnets that are competitive to the ones made by the established route of hot deformation via die-upsetting. Nevertheless, homogeneous densification of the powder flakes in the center of the sample allows for a conclusion on how Flash SPS parameters can be tuned to control grain growth of primary grains and related magnetic properties. In the following sections, only results from the center of the sample and magnetic properties perpendicular to the compaction direction are considered for the discussion.

3.3. Fine Tuning of Magnetic Properties of Flash SPS Samples by Variation of the Preheating Conditions

Two hypotheses were investigated to evaluate the potential of Flash SPS for tuning the magnetic properties toward high anisotropy. First, the dwell time for pre-sintering at 500 °C was varied to 30 and 120 s, with the aim of achieving differently pronounced sintering necks while keeping the grain growth negligible. It was assumed that larger sintering necks between primary particles might retard grain growth during the dynamic Flash SPS deformation. The second aspect was to better understand the influence of the preheating temperature before starting the Flash SPS cycle. Therefore, the pre-sintered samples were Joule heated in the Flash SPS setup to a defined temperature in the range between 251 and 600 °C (measured by pyrometer). After heating to the specific temperature, this temperature was held for 120 s to homogeneously heat the samples before applying the power pulse, which was kept constant for all samples (35 kW, 30 s). Preheating was done below the melting temperature of the ternary eutectic phase of 655 °C,^[34–36] to already minimize the grain growth during preheating. A DSC measurement was done to check the possible formation of a melting phase during preheating. A clearly pronounced exothermic peak was observed at a temperature of 550 °C (Figure S3, Supporting Information). Sawatzki^[62] observed a similar exothermic peak at 555 °C and explained this peak as the crystallization of residual amorphous phase in the starting powder rather than by the formation of a melting phase. It was argued that the amount of melting phase might be too low to cause a clearly pronounced DSC peak. Due to pre-sintering being done at 500 °C in the present study, possible residual amorphous phase would be still present when starting the preheating of the Flash SPS cycle.

For the subsequent discussion of microstructure evolution, the extreme cases (preheating at 251 and 600 °C) were considered. Figure 6 and 7 show the microstructure (fractured surface and polished surface) of the sample which was preheated to 251 °C before Flash SPS. Figure 8 and 9 show the related microstructures in the case of preheating to 600 °C. When looking at the microstructures, it becomes obvious that dwell time of pre-sintering and temperature of preheating before Flash SPS play distinct roles for microstructure evolution. When preheating is done at 251 °C, grain growth and grain alignment after Flash SPS is significantly less pronounced (Figure 6 and 7). By trend, anisotropic grain growth seems to be slightly improved when the sample was pre-sintered at 500 °C for 120 s, as shown by the appearance of platelike grains in Figure 6b. Nevertheless, a lot of grains are still oriented in different spatial directions, which might explain the low-magnetic anisotropy discussed later. Contrarily, when increasing the preheating temperature to 600 °C, significant grain growth and grains well aligned perpendicular to the deformation direction appear (Figure 8 and 9). Nevertheless, even in this case, the microstructure differs from the optimized high-performing magnets made by die-upsetting, giving room for further improvements in Flash SPS process.^[31,38,62] There are, however, some microstructural features which must be considered carefully when further optimizing the Flash SPS technology for magnet manufacturing. In addition to areas where the grains look already quite optimum for achieving

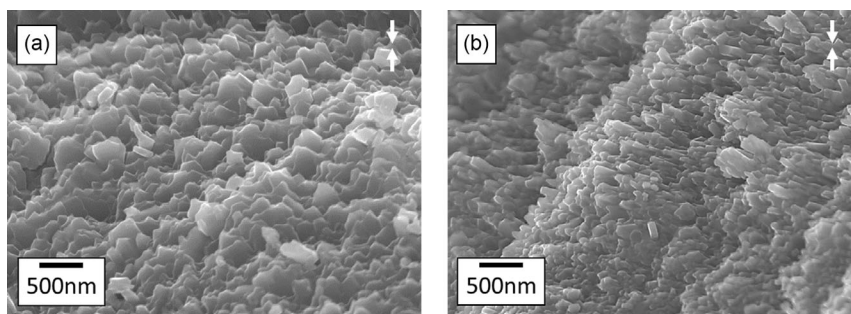


Figure 6. Fractured surface of samples which were preheated before Flash SPS to 251 °C. a) Sample pre-sintered at 500 °C for 30 s (A-30_251) and b) sample pre-sintered at 500 °C for 120 s (B-120_251). The pressure direction is given by the white arrows.

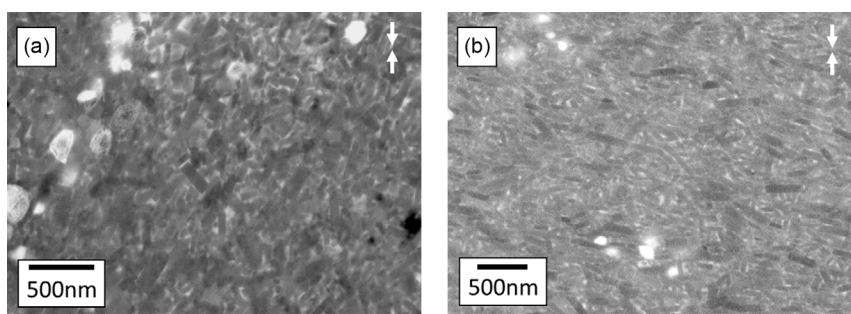


Figure 7. Alignment of grains of samples which were preheated before Flash SPS to 251 °C. a) Sample pre-sintered at 500 °C for 30 s (A-30_251) and b) sample pre-sintered at 500 °C for 120 s (B-120_251). The pressure direction is given by the white arrows.

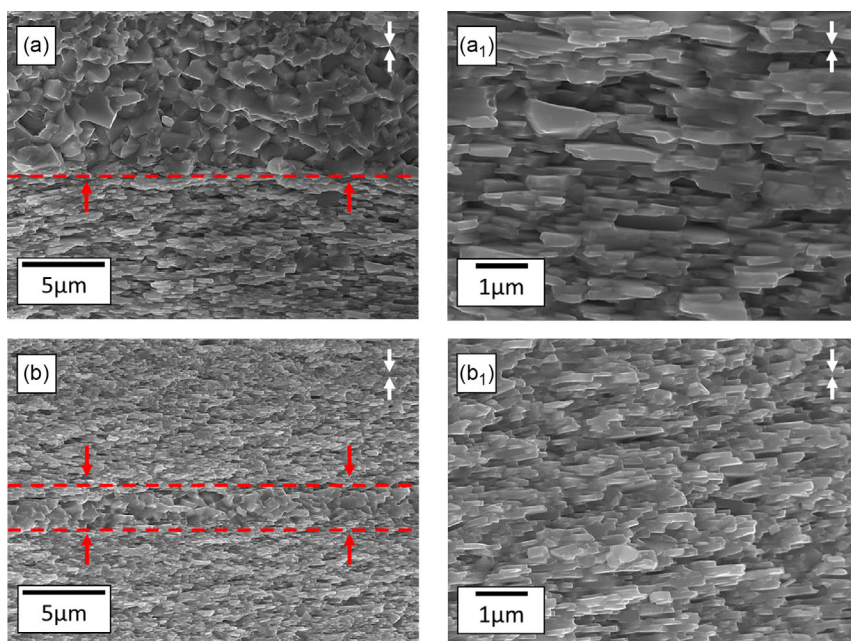


Figure 8. Fractured surface of samples which were preheated before Flash SPS to 600 °C. a, a₁) Sample pre-sintered at 500 °C for 30 s (A-30_600) and b, b₁) sample pre-sintered at 500 °C for 120 s (B-120_600). The pressure direction is given by the white arrows. The red arrow and the dashed line show regions with abnormal grain growth.

high-magnetic anisotropy, onset of abnormal grain growth was observed, which was clearly more pronounced when pre-sintering was done with lower dwell time (Figure 8a,b).

Similar abnormal grain growth was also reported in the fundamental works of Castle et al. describing the potential of Flash SPS for manufacturing anisotropic magnets for the first time.^[42,58]

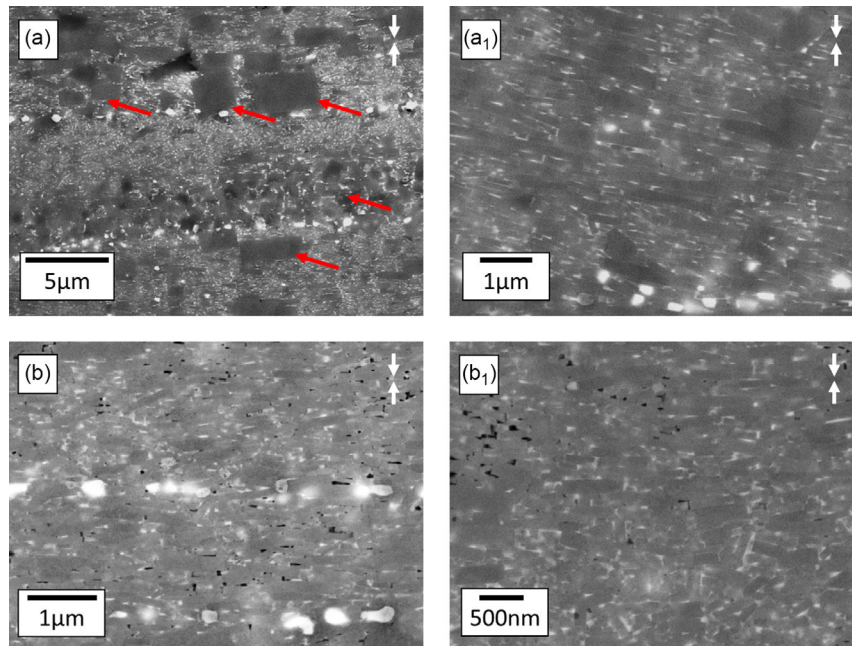


Figure 9. Alignment of grains after Flash SPS step for samples preheated to 600 °C. a,a₁) Sample pre-sintered at 500 °C for 30 s (A-30_600); b,b₁) Sample pre-sintered at 500 °C for 120 s (B-120_600). The red arrows in (a₁) highlight the regions with abnormal grain growth. The pressure direction is given by the white arrows.

Abnormal grain growth was also reported by Zhihua et al.^[64] Here, the authors did the die-upsetting of Nd–Fe–B magnets in a conventional FAST/SPS device. A remarkable result of the present study is that formation of better pronounced sintering necks by increasing the dwell time during pre-sintering obviously seems to be an effective measure to suppress abnormal grain growth to a certain degree. When discussing abnormal grain growth during Flash SPS, it must be considered that the effect is superimposed by large grains which are already formed on the surface of the powder flakes facing away from the copper

wheel during melt spinning. Nevertheless, lower magnetic properties of samples pre-sintered at 500 °C for 30 s indicate that additional abnormal grain growth appears during Flash SPS.

Figure 10 shows the demagnetization curves along the easy magnetization axis of all Flash SPS samples produced in the present work—additional measurement along the perpendicular direction to the applied pressure is given to emphasize the anisotropic behavior. The measurements confirm the clear influence of the pre-sintering and preheating conditions on the magnetic properties when applying constant Flash SPS

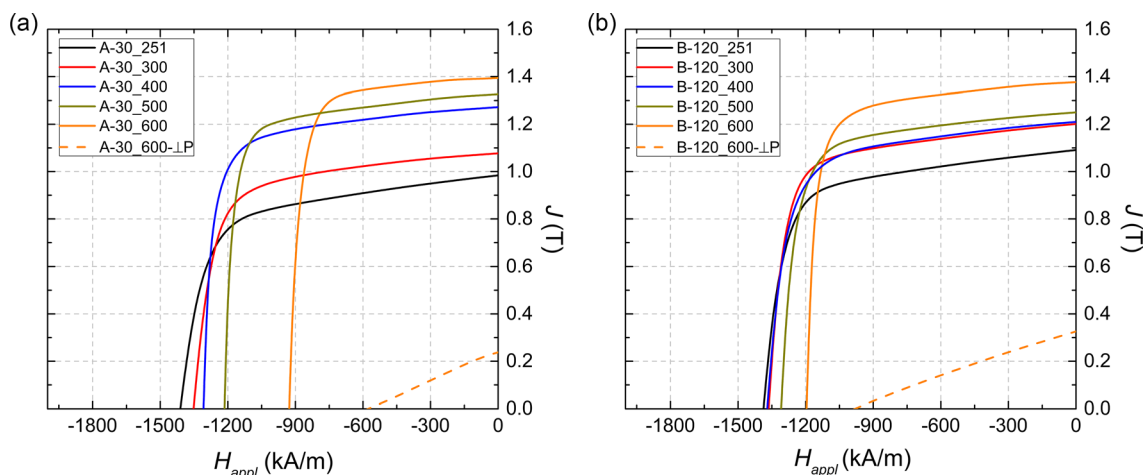


Figure 10. Demagnetization curves of both Flash SPS series a) A series with pre-sintering at 500 °C for 30 s b) B series with pre-sintering at 500 °C for 120 s along the easy magnetization axis, i.e., parallel to the applied pressure. Additional measurement along the hard magnetization axis (perpendicular to the applied pressure—both Tangent and Radial orientations show overlapping curves) for the samples processed at higher temperature is also given. The magnetic measurements are from the center part of the Flash SPS samples.

parameters (35 kW, 30 s, and 32 MPa). There is a general trend that the increase of the preheating temperature leads to a higher-deformation degree (smaller sample height) in the macroscopic scale while causing a coarsening and a more pronounced alignment of the grains in micro- and nanoscale, which explains the decrease in coercivity and enhancement in remanence, respectively. It is obvious from the temperature–power–displacement curves (Figure S6, Supporting Information) that—due to the applied load of 32 MPa required for the operation of our FAST/SPS setup—deformation and therefore also anisotropic grain growth already starts during this preheating step, most clearly pronounced in the case of samples preheated to 500 and 600 °C. With respect to literature,^[34,36] it is likely that no liquid phase has been formed during preheating, which is expected to further promote grain growth. Nevertheless, in the final Flash SPS step, formation of a liquid phase is quite probable since the temperature clearly exceeds 700 °C as captured by the pyrometer measurement near to the sample.

It becomes obvious that pre-sintering of the powder compacts at 500 °C with longer dwell time of 120 s leads to a reduced scattering of the demagnetization curves. In addition, the higher coercivity of samples from the B-series—especially for samples preheated to 500 and 600 °C—indicate that longer pre-sintering of the powder compacts at 500 °C retards abnormal grain growth in the subsequent Flash SPS cycle. The formation of the larger, blocky-like grains observed in Figure 9a is assumed to be the main reason for the strong decrease of coercivity in the case of the A-series sample preheated to 600 °C.

For sake of completeness, Table 2 summarizes the coercivity H_{cJ} , remanence B_r , and maximum energy $(BH)_{max}$ of all samples produced in this study. Furthermore, the height reduction after the Flash SPS cycle is calculated. We omitted giving the degree of deformation as these samples start from a porous compact. Nevertheless, monotonous increase of height reduction and therefore sample deformation with increasing preheating temperature explains the increase of remanence as function of preheating temperature. Comparing the figures of merit for the different magnets, if one chooses as selection criteria solely based on the energy product, the A-30_600 sample shows the

highest value, 364 kJm⁻³, since the $(BH)_{max}$ is mainly related to remanence for these high coercive magnets. However, taking into consideration the coercivity as well, the magnet that shows a good balance between all three figures of merit is B-120_600, with coercivity of 1195 kAm⁻¹ (nearly 300 kAm⁻¹ higher than the counterpart sample in the A series), remanence of 1.37 T and energy product of 351 kJm⁻³.

Compared to the literature, a significant improvement was achieved for anisotropic Nd–Fe–B magnets made by Flash SPS. Sample A-30_300 is preferentially suitable for benchmarking, since this sample was produced with the same parameter set than the sample with the best magnetic properties of our previous work.^[44] In this study, the best sample had a coercivity H_{cJ} of 1483 kAm⁻¹, a remanence B_r of 1.18 T, and a maximum energy product $(BH)_{max}$ of 264 kJm⁻³. Similar properties were also reported in the pioneering Flash SPS work of Castle et al.^[42] Here, the best sample—also made from MQU-F powder—achieved a coercivity of 1438 kAm⁻¹, remanence of 1.16 T and maximum energy-product of 230 kJm⁻³. As general reference, a die-upset magnet from the standard production of our industrial partner WILO SE, also starting from MQU-F powder, shows coercivity of 1342 kAm⁻¹, a remanence of 1.30 T, and a maximum energy product of 323 kJm⁻³.^[44] Extending the comparison to the conventional hot-pressing followed by hot-deformation process, the work of Khlopkov et al. has shown that increasing the height reduction leads to an improvement in remanence and a decrease in coercivity, similar to observed for the Flash SPS samples (Table 2).^[18,31] After hot-pressing, a remanence of 0.88 T and coercivity of 1750 kAm⁻¹ was reported, while a remanence enhancement to 1.34 T and a decay in coercivity to 955 kAm⁻¹ was obtained after hot deformation with height reduction of 76%.^[18,31] Considering the sample with highest height reduction obtained in our work, 71.3%, we observe a slightly higher remanence of 1.37 T and higher coercivity of 1195 kAm⁻¹ in comparison to the former study of Khlopkov et al. The higher combination of magnetic properties, remanence, and coercivity highlights the potential of Flash SPS to obtain high-performance Nd–Fe–B magnets in relation to well-established route of hot-pressing/deformation.

Beyond the anisotropic magnetic response obtained by the volume magnetization measurements, we have analyzed the magnetic domain structure to gain further insight on the local texture created during the Flash SPS process. With this aim, the center part of the samples with lowest and highest remanence for each sample series was selected. The Kerr micrograph of the samples pre-sintered at the lowest temperature (Figure 11, lowest remanence), 251 °C, revealed two main distinct areas. The magnetic domains within the area highlighted in red, in both Figure 11a,b, could not be resolved using Kerr microscopy, thus MFM has been used in these regions: Figure 11a₁,a₂,b₁,b₂. The formation of fine magnetic domain clusters have been observed, as denoted by the phase contrast change within this region (Figure 11a₁), evidencing the random orientation of nanometer-sized grains. Comparatively, the area highlighted in black can be resolved using Kerr, and in more detail by MFM (Figure 11a₂), showing the appearance of defined maze-like domain structure. This magnetic domain arrangement can be directly linked to the magnetostatic interaction of grains showing local texture, as extensively studied by Khlopkov et al.^[18,31] Similar behavior for both series of

Table 2. Coercivity H_{cJ} , remanence B_r , and energy product $(BH)_{max}$ of both Flash SPS series. Sample height after Flash SPS is also given. The initial height of the samples was 8.2 ± 0.1 mm. The magnetic properties were derived from Figure 10.

Sample code	H_{cJ} [kAm ⁻¹]	B_r [T]	$(BH)_{max}$ [kJm ⁻³]	Sample height [mm]	Height reduction [%]
A-30_251	1412	0.98	169	4.02	51.0
A-30_300	1353	1.07	209	2.96	63.9
A-30_400	1305	1.27	295	2.66	67.6
A-30_500	1215	1.32	324	2.57	68.6
A-30_600	927	1.39	364	2.37	71.1
B-120_251	1390	1.09	212	3.32	59.5
B-120_300	1364	1.20	262	2.92	64.4
B-120_400	1370	1.21	266	2.78	66.1
B-120_500	1309	1.25	285	2.65	67.7
B-120_600	1195	1.37	351	2.35	71.3

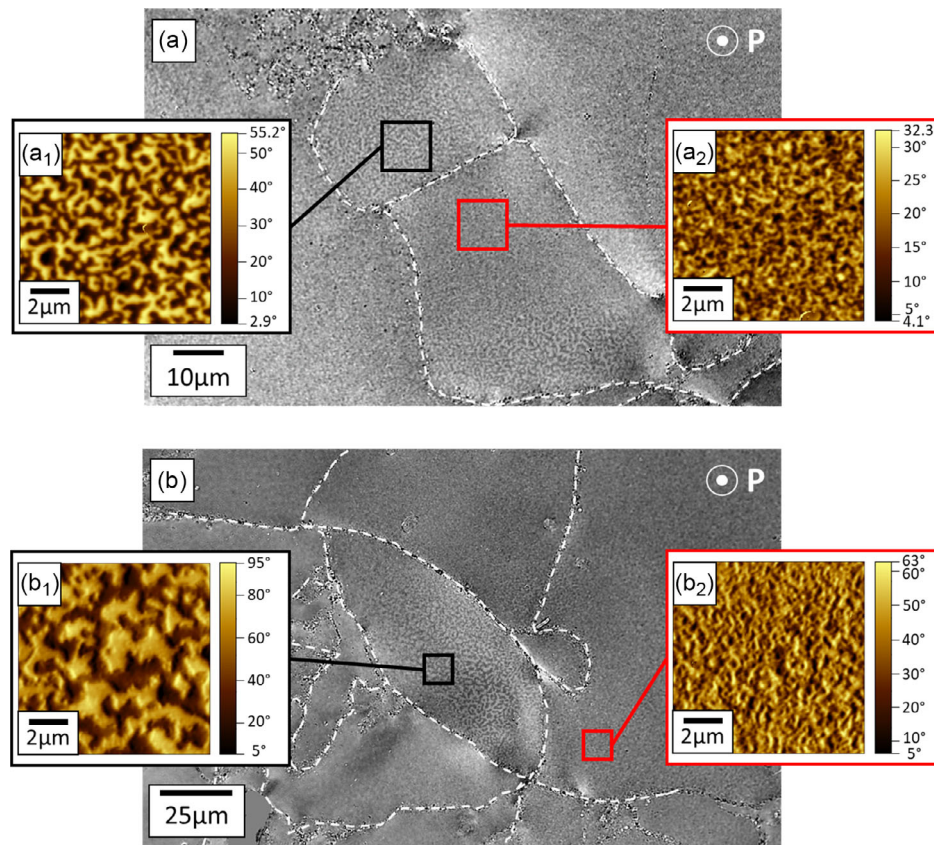


Figure 11. Kerr micrographs of samples after the Flash SPS step which were preheated before Flash SPS to 251 °C: a) Sample pre-sintered at 500 °C for 30 s (A-30_251); b) sample pre-sintered at 500 °C for 120 s (B-120_251). Insets show a higher magnification image obtained by magnetic force microscopy (MFM) of the selected areas (a_1 , a_2 and b_1 , b_2). The flake boundaries are highlighted with dashed lines. Please, note the different scale bars in both Kerr micrographs. The plane view is along the pressure direction, easy magnetization axis.

samples can be seen, which indicates inhomogeneity on the deformation degree within the sample, even across a few micrometers. It worth noting that the scale of mazelike domains and the phase-shift degree increases with the degree of texture (Figure 11b, b_1 , b_2), as confirmed by the increase in remanence of the sample produced at lower flash SPS temperature of series B in comparison with series A.

In contrast to the samples produced at the lowest Flash SPS temperature, the samples processed at the highest temperature, 600 °C, show large areas containing mazelike domain structure, confirming the high texture degree of these samples (Figure 12a,b), as observed from the magnetization measurements. In the sample of series A, the inset (Figure 12a₁) shows a higher magnification, that one can observe the coexistence of mazelike domains, arising from the textured nanocrystalline grains, and larger grains, emphasized by the red arrows, displaying multi-domain state. These micrometer-sized grains, above the critical single domain ($D_c \approx 300$ nm for $\text{Nd}_2\text{Fe}_{14}\text{B}$), can be associated to the decrease in coercivity observed for this sample, as discussed previously. These multi-domain state grains were not observed in the sample with longer pre-sintering times, series B, showing a more homogeneous distribution of interaction domains (Figure 12b, b_1 , b_2 , Kerr and MFM results), in accordance to the SEM observations and the

higher coercivity obtained in comparison with the sample with coarser microstructure.

4. Conclusions and Outlook

In the present work, Nd-Fe-B magnets with well-pronounced anisotropic magnetic properties were produced via Flash SPS. A specific focus of the study lay on the understanding of how the formation of sintering necks already formed during pre-sintering of the powder compacts influenced the microstructure evolution during Flash SPS. Therefore, the powder compacts were pre-sintered via FAST/SPS at 500 °C with varying dwell time of 30 and 120 s. It was found that increasing the dwell time to 120 s reduced the risk of abnormal grain growth during hot deformation via Flash SPS. A second aspect was to study the influence of preheating the samples before Flash SPS on the final microstructure and magnetic properties after Flash SPS. The study shows that preheating at temperatures in the range of 400–600 °C is recommended to take full advantage of Flash SPS. Our results reveal that deformation and therefore also anisotropic grain growth already starts during the preheating step triggered by the applied load of 32 MPa. Initiation of anisotropic

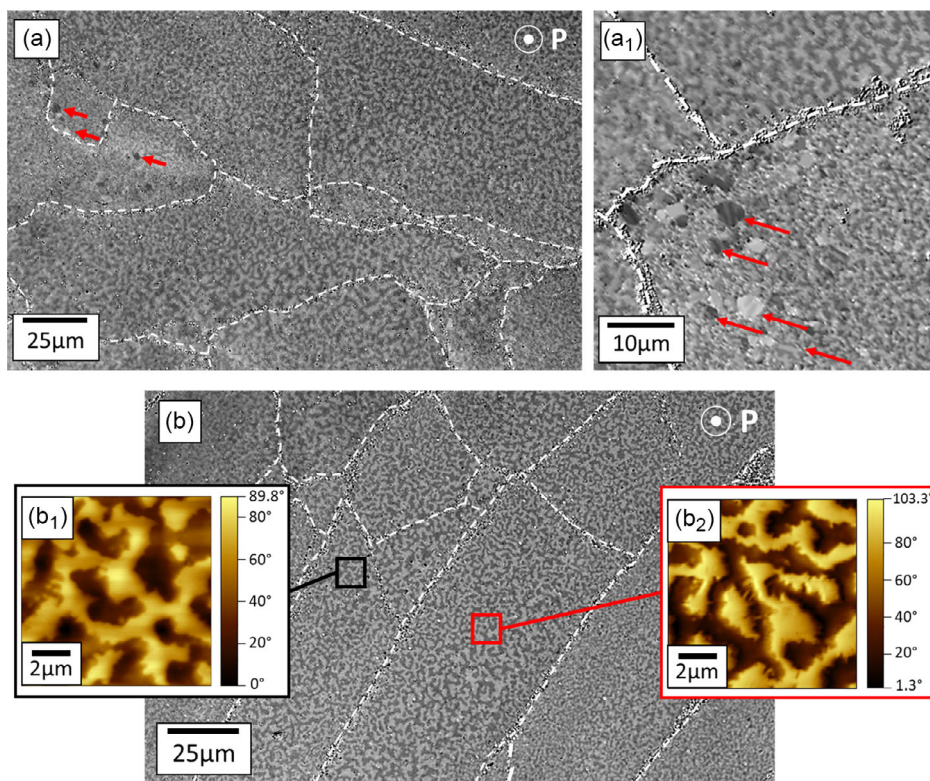


Figure 12. Kerr microscopy of samples after the Flash SPS step which were preheated before Flash SPS to 600 °C: a) Sample pre-sintered at 500 °C for 30 s (A-30_600); b) sample pre-sintered at 500 °C for 120 s (B-120_600). Insets show a higher magnification image obtained by Kerr (a_1) and MFM (b_1 and b_2) of the selected areas. The flake boundaries are highlighted with dashed lines and multidomain grains are emphasized with red arrows. The plane view is along the pressure direction, easy magnetization axis.

grain growth already during preheating seems to support the evolution of a clearly pronounced anisotropic microstructure during Flash SPS. From a technological perspective, the preheating step leads to overall cycle times of several minutes, which cannot compete with automated hot-pressing and die-upset technology established in industry. To overcome this drawback, separate preheating and cooling zones as used in conventional FAST/SPS and hot-pressing plants to increase production capacity^[65] could be adapted to Flash SPS technology in future.

Compared to our former study,^[44] a clear improvement of magnetic properties was achieved and remanence above 1.35 T demonstrates the general potential of Flash SPS as alternative hot-deformation method for nanocrystalline Nd–Fe–B magnets. The most balanced property profile in this work was achieved by the sample B-120_600, which was pre-sintered at 500 °C for 120 s and preheated before Flash SPS to 600 °C. The sample shows a coercivity H_{cJ} of 1195 kAm⁻¹, a remanence B_r of 1.37 T, and a maximum energy product $(BH)_{max}$ of 350 kJm⁻³. Nevertheless, further improvement of the Flash SPS parameters accompanied by introducing an outer die in the Flash SPS setup are necessarily required to go a step further.

Even at this premature stage of development, Flash SPS put some technological aspects in perspective, which are difficult to achieve by established hot-deformation technologies like die-upsetting. Flash SPS enables to start from porous powder compacts, which might enable to completely omit the pre-sintering

step in future. Contrarily, the present work shows that the pre-sintering step and in especial the formation of sintering necks between the primary particles plays a significant role for tuning the microstructure of Nd–Fe–B magnets hot deformed via Flash SPS. Therefore, further studies are required to conclusively decide on the necessity of pre-sintering. A second promising aspect is the possibility to apply Flash SPS for the direct recycling of scrap from hot-deformed Nd–Fe–B magnets. Recently, we demonstrated the manufacturing of anisotropic Nd–Fe–B magnets with a coercivity H_{cJ} of 667 kAm⁻¹, a remanence B_r of 1.16 T and a maximum energy product $(BH)_{max}$ of 202 kJm⁻³ starting from 100% magnet scrap.^[44] Therefore, figuring out the potential of Flash SPS for direct recycling of magnet scrap will be one of the main focus of our future work.

Supporting Information

Supporting Information is available from the Wiley Online Library or from the author.

Acknowledgements

This work was supported by the German Research Foundation (DFG) within the Priority Program “Manipulation of matter controlled by an electric and magnetic field” (SPP 1959) under the grant numbers BR 3418/1-2 and GU 514/8-2, and within the CRC/TRR 270 HoMMage (Project-ID

405553726). Furthermore, the authors highly acknowledge the experimental support of Ralf Steinert when operating our FAST/SPS and Flash SPS setups.

Open Access funding enabled and organized by Projekt DEAL.

Conflict of Interest

The authors declare no conflict of interest.

Data Availability Statement

The data that support the findings of this study are available from the corresponding author upon reasonable request.

Keywords

anisotropic magnet, flash spark plasma sintering, nanocrystalline Nd-Fe-B, Nd-Fe-B magnets

Received: February 22, 2023

Revised: April 26, 2023

Published online: May 16, 2023

-
- [1] O. Gutfleisich, M. A. Willard, E. Brück, C. H. Chen, S. G. Sankar, J. Ping Liu, *Adv. Mater.* **2011**, *23*, 821.
- [2] Y. Matsuura, *J. Magn. Magn. Mater.* **2006**, *303*, 344.
- [3] S. Sugimoto, *J. Phys. D: Appl. Phys.* **2011**, *44*, 64001.
- [4] Y. Yang, A. Walton, R. Sheridan, K. Güth, R. Gauß, O. Gutfleisich, M. Buchert, B.-M. Steenari, T. Van Gerven, P. T. Jones, K. Binnemanns, *J. Sustainable Metall.* **2017**, *3*, 122.
- [5] S. Hiroswawa, Y. Matsuura, H. Yamamoto, S. Fujimura, M. Sagawa, *J. Appl. Phys.* **1986**, *59*, 873.
- [6] T. G. Woodcock, Y. Zhang, G. Hrkac, G. Ciuta, N. M. Dempsey, T. Schrefl, O. Gutfleisich, D. Givord, *Scr. Mater.* **2012**, *67*, 536.
- [7] T. G. Woodcock, F. Bittner, T. Mix, K.-H. Müller, S. Sawatzki, O. Gutfleisich, *J. Magn. Magn. Mater.* **2014**, *360*, 157.
- [8] E. Alonso, A. M. Sherman, T. J. Wallington, M. P. Everson, R. Field, R. Roth, R. E. Kirchain, *Environ. Sci. Technol.* **2012**, *46*, 3406.
- [9] K. Loewe, D. Benke, C. Kübel, T. Lienig, K. P. Skokov, O. Gutfleisich, *Acta Mater.* **2017**, *124*, 421.
- [10] T. Helbig, K. Loewe, S. Sawatzki, M. Yi, B.-X. Xu, O. Gutfleisich, *Acta Mater.* **2017**, *127*, 498.
- [11] K. Bourzac, *Technol. Rev.* **2011**, *114*, 58.
- [12] J. H. Rademaker, R. Kleijn, Y. Yang, *Environ. Sci. Technol.* **2013**, *47*, 10129.
- [13] R. Gauss, G. Homm, O. Gutfleisich, *J. Ind. Ecol.* **2016**, *21*, 1291.
- [14] R. Gauss, C. Burkhardt, F. Carencotte, M. Gasparon, O. Gutfleisich, I. Higgins, M. Karajić, A. Klossek, M. Mäkinen, B. Schäfer, R. Schindler, B. Veluri, A Report by the Rare Earth Magnets and Motors Cluster of the European Raw Materials Alliance, Berlin, <https://eitrawmaterials.eu/wp-content/uploads/2021/09/ERMA-Action-Plan-2021-A-European-Call-for-Action.pdf> (accessed: December 2021).
- [15] H. Sepehri-Amin, T. Ohkubo, K. Hono, *Acta Mater.* **2013**, *61*, 1982.
- [16] T. T. Sasaki, T. Ohkubo, Y. Takada, T. Sato, A. Kato, Y. Kaneko, K. Hono, *Scr. Mater.* **2016**, *113*, 218.
- [17] A. Kirchner, J. Thomas, O. Gutfleisich, D. Hinz, K.-H. Müller, L. Schultz, *J. Alloys Compd.* **2004**, *365*, 286.
- [18] K. Khlopkov, O. Gutfleisich, D. Hinz, K.-H. Müller, L. Schultz, *J. Appl. Phys.* **2007**, *102*, 023912.
- [19] T. G. Woodcock, Q. M. Ramasse, G. Hrkac, T. Shoji, M. Yano, A. Kato, O. Gutfleisich, *Acta Mater.* **2014**, *77*, 111.
- [20] I. Dirba, S. Sawatzki, O. Gutfleisich, *J. Alloys Compd.* **2014**, *589*, 301.
- [21] S. Sawatzki, I. Dirba, H. Wendrock, L. Schultz, O. Gutfleisich, *J. Magn. Magn. Mater.* **2014**, *358–359*, 163.
- [22] K. Hioki, *Sci. Technol. Adv. Mater.* **2021**, *22*, 72.
- [23] D. Brown, B.-M. Ma, Z. Chen, *J. Magn. Magn. Mater.* **2002**, *248*, 432.
- [24] O. Gutfleisich, *J. Phys. D* **2000**, *33*, R157.
- [25] G. Sarriegui, J. M. Martín, M. Ipatov, A. P. Zhukov, J. Gonzalez, *IEEE Trans. Magn.* **2018**, *54*, 2103105.
- [26] O. Gutfleisich, I. R. Harris, *J. Phys.* **1996**, *29*, 2255.
- [27] O. Gutfleisich, G. Drazic, C. Mishima, Y. Honkura, *IEEE Trans. Magn.* **2002**, *38*, 2958.
- [28] Y. Honkura, C. Mishima, N. Hamada, O. Gutfleisich, *J. Magn. Magn. Mater.* **2005**, *290–291*, 1282.
- [29] L. Schultz, J. Wecker, E. Hellstern, *J. Appl. Phys.* **1987**, *61*, 3583.
- [30] A. Bollero, O. Gutfleisich, G. Drazic, K. H. Müller, L. Schultz, *J. Appl. Phys.* **2002**, *91*, 8159.
- [31] K. Khlopkov, O. Gutfleisich, R. Schäfer, D. Hinz, K.-H. Müller, L. Schultz, *J. Magn. Magn. Mater.* **2004**, *272–276*, E1937.
- [32] J. Song, M. Yue, J. Zuo, Z. Zhang, W. Liu, D. Zhang, J. Zhang, Z. Guo, W. Li, *J. Rare Earths* **2013**, *31*, 674.
- [33] J. J. Croat, *Rapidly Solidified Neodymium-Iron-Boron Permanent Magnets*, Woodhead Publishing Series in Electronic and Optical Materials, Elsevier, Cambridge, MA **2018**.
- [34] G. Schneider, E.-T. Henig, G. Petzow, H. Stadehnaier, *Z. Metallkd.* **1986**, *77*, 755.
- [35] B. Grieb, E.-T. Henig, G. Schneider, G. Knoch, G. Petzow, D. de Mooij, *Powder Metall.* **1992**, *35*, 221.
- [36] K. G. Knoch, B. Reinsch, G. Petzow, *Z. Metallkd.* **1994**, *85*, 350.
- [37] W. Grünberger, D. Hinz, A. Kirchner, K.-H. Müller, L. Schultz, *J. Alloys Compd.* **1997**, *257*, 293.
- [38] O. Gutfleisich, A. Kirchner, W. Grünberger, D. Hinz, H. Nagel, P. Thompson, J. N. Chapman, K. H. Müller, I. R. Harris, L. Schultz, *J. Phys. D* **1998**, *31*, 807.
- [39] B. Ruszkiewicz, T. Grimm, I. Ragai, L. Mears, J. T. Roth, *J. Manuf. Sci. Eng.* **2017**, *139*, 110801.
- [40] O. Guillon, C. Elsässer, O. Gutfleisich, J. Janek, S. Korte-Kerzel, D. Raabe, C. Volkert, *Mater. Today* **2018**, *21*, 527.
- [41] N. K. Dimitrov, Y. Liu, M. F. Horstemeyer, *Mech. Adv. Mater. Struct.* **2002**, *5*, 705.
- [42] E. Castle, R. Sheridan, W. Zhou, S. Grasso, A. Walton, M. J. Reece, *Sci. Rep.* **2017**, *7*, 11134.
- [43] L. Leich, A. Röttger, M. Krengel, W. Theisen, *J. Sustainable Metall.* **2019**, *5*, 107.
- [44] T. Prasad Mishra, L. Leich, M. Krengel, S. Weber, A. Röttger, M. Bram, *Adv. Eng. Mater.* **2023**, *25*, 2201027.
- [45] R. Orrú, R. Licheri, A. M. Locci, A. Cincotti, G. Cao, *Mater. Sci. Eng., R* **2009**, *63*, 127.
- [46] L. Leich, A. Röttger, W. Theisen, M. Krengel, *J. Magn. Magn. Mater.* **2018**, *460*, 454.
- [47] L. Leich, A. Röttger, R. Kuchenbecker, W. Theisen, *J. Mater. Sci.: Mater. Electron.* **2020**, *31*, 20431.
- [48] O. Guillon, O. J. Gonzalez-Julian, B. Dargatz, T. Kessel, G. Schierning, J. Räthel, M. Hermann, *Adv. Eng. Mater.* **2014**, *16*, 830.
- [49] H. Wuest, L. Bommer, T. Weißgärber, B. Kieback, *J. Magn. Magn. Mater.* **2015**, *392*, 74.
- [50] T. Wang, M. Yue, Y. Li, M. Tokita, Q. Wu, D. Zhang, J. Zhang, *IEEE Magn. Lett.* **2015**, *6*, 1.
- [51] M. Yue, J. Zhang, M. Tian, *J. Appl. Phys.* **2006**, *99*, 08B502.
- [52] M. Yue, A. Cao, G. Wang, W. Liu, J. Zhang, *Phys. Status Solidi A* **2007**, *204*, 4149.
- [53] W. Q. Liu, Z. Z. Cui, X. F. Yi, M. Yue, Y. B. Jiang, D. T. Zhang, J. X. Zhang, X. B. Liu, *J. Appl. Phys.* **2010**, *107*, 09A719.
- [54] Z. Hu, L. Chu, J. Li, Y. Liu, *J. Rare Earths* **2011**, *29*, 660.

- [55] Y. L. Huang, Z. W. Liu, X. C. Zhong, H. Y. Du, D. C. Zeng, *Powder Metall.* **2012**, 55, 124.
- [56] W. Kaszuwara, M. Leonowicz, B. Michalski, M. Lis, *EPJ Web Conf.* **2013**, 40, 06002.
- [57] S. Grasso, T. Saunders, H. Porwal, O. Cedillos-Barraza, D. D. Jayaseelan, W. E. Lee, M. J. Reece, *J. Am. Ceram. Soc.* **2014**, 97, 2405.
- [58] E. Castle, S. Grasso, M. Reece, R. Sheridan, A. Walton, *J. Magn. Magn. Mater.* **2016**, 417, 279.
- [59] S. Hirose, Y. Matsuura, H. Yamamoto, S. Fujimura, M. Sagawa, *J. Appl. Phys.* **1991**, 69, 5844.
- [60] H. Sepehri-Amin, J. Liu, T. Ohkubo, K. Hioki, A. Hattori, K. Hono, *Scr. Mater.* **2013**, 69, 647.
- [61] J. Liu, H. Sepehri-Amin, T. Ohkubo, K. Hioki, A. Hattori, T. Schrefl, K. Hono, *Acta Mater.* **2013**, 61, 5387.
- [62] S. Sawatzki, C. Kübel, S. Ener, O. Gutfleisch, *Acta Mater.* **2016**, 115, 354.
- [63] S.-K. Kim, S. Hwang, J.-H. Lee, *J. Magn. Magn. Mater.* **2019**, 486, 165257.
- [64] H. Zhihua, C. Linhua, L. Jun, L. Ying, *J. Rare Earths* **2011**, 29, 660.
- [65] J. Hennicke, H. U. Kessel, T. Kessel, H. Neess, *DKG* **2019**, 96, E1.